Chemical Science

ROYAL SOCIETY OF CHEMISTRY

EDGE ARTICLE

View Article Online
View Journal | View Issue

Cite this: *Chem. Sci.*, 2022, **13**, 8052

All publication charges for this article have been paid for by the Royal Society of Chemistry

Steam-assisted crystallization of highly dispersed nanosized hierarchical zeolites from solid raw materials and their catalytic performance in lactide production†

Zhe Ma,[a] Qiang Zhang,[a] Lin Li,[b] Mengyang Chen,[a] Junyan Li[ac] and Jihong Yu *[ad]

Received 20th May 2022
Accepted 20th June 2022

DOI: 10.1039/d2sc02823a

rsc.li/chemical-science

A solvent-free route based on solid raw materials affords higher product yield and lower waste production compared to the traditional hydrothermal synthesis. However, the as-made zeolites usually present blocky aggregation states, limiting their mass transfer and exposure of active sites in catalytic applications. Herein, highly dispersed nanosized hierarchical Beta zeolites with varied Si/Al ratios were prepared *via* steam-assisted crystallization from ball-milled solid raw materials. Thanks to the sufficient mixing of solid raw materials and favorable migration of solid mixture, nanosized Beta zeolites are obtained that are assembled from nanoparticles (~15 nm) and possess abundant interconnected intraparticle mesopores. The strategy can also be extended to synthesize nanosized hierarchical ZSM-5 zeolites. The as-prepared Beta zeolite (Si/Al = 10) exhibits outstanding catalytic performance in conversion of lactic acid to lactide (as high as 77.5% in yield). This work provides avenues for simple and cost-efficient synthesis of highly dispersed nanosized hierarchical zeolites, promising their important catalytic applications.

Introduction

Zeolites with well-defined micropores, tunable active sites, and high thermal/hydrothermal stabilities are widely used in adsorption, separation, and catalysis.[1] Particularly, Beta (***BEA**-type) and ZSM-5 (**MFI**-type) zeolites are excellent shape-selective catalysts in many industrial catalytic reactions, such as fluid catalytic cracking, methanol to hydrocarbons, and benzene alkylation, *etc.*[2] The conventional synthesis strategies of zeolites include hydrothermal, ionothermal, and solvothermal routes, which require the presence of a large amount of solvents (water, organic solvents, or ionic liquids) for fast mass transfer of reactants, eventually resulting in a low product yield of zeolites and the generation of polluted wastes.[3] Therefore, developing a cost-effective method for the synthesis of zeolites in the absence of solvents is of great significance from the both academic and industrial points of view.

To this end, Xiao's group developed a solvent-free route for the synthesis of zeolites by mixing, grinding, and heating starting solid raw materials.[4] Compared to the traditional hydrothermal synthesis, the lack of solvents not only significantly increases the product yield of zeolites, but also greatly reduces waste production. Such a solvent-free route has been used for the synthesis of a variety of silicoaluminophosphate,[5] aluminophosphate,[6] and aluminosilicate[7] zeolites with different topological structures types. However, grinding and heating the solid raw mixture under solvent-free conditions generally causes serious aggregation of zeolite products due to inhomogeneous mixing and low migration rate of solid mixture during the crystallization process, which results in poor product uniformity and texture properties.[8] The above drawbacks of zeolites prepared by solvent-free route cause low utilization of acid sites and severe diffusion limitation in the catalytic reaction process, and ultimately lead to the inferior catalytic performance.[9] Therefore, the development of a facile synthesis strategy to prepare well-dispersed zeolites based on solid raw materials, particularly with nanosized or hierarchical structures, is highly desired for catalytic applications.

It is well known that the steam-assisted crystallization (SAC) strategy from dense-gel has been developed to prepare hierarchical zeolites formed with nanocrystals, in which the amount of organic templates is lower than that in conventional synthesis approaches.[10] For example, Zhang *et al.* reported the

[a]*State Key Laboratory of Inorganic Synthesis and Preparative Chemistry, College of Chemistry, Jilin University, 2699 Qianjin Street, Changchun 130012, P. R. China. E-mail: jihong@jlu.edu.cn*

[b]*Electron Microscopy Center, Jilin University, 2699 Qianjin Street, Changchun 130012, P. R. China*

[c]*Center for High-resolution Electron Microscopy (ChEM), School of Physical Science and Technology, ShanghaiTech University, 393 Middle Huaxia Road, Pudong, Shanghai 201210, P. R. China*

[d]*International Center of Future Science, Jilin University, 2699 Qianjin Street, Changchun 130012, P. R. China*

† Electronic supplementary information (ESI) available. See https://doi.org/10.1039/d2sc02823a

synthesis of hierarchical Beta with a small amount of tetraethylammonium hydroxide ($TEAOH/SiO_2 = 0.06$) by the SAC method.[11] Furthermore, the concentrated gel system is beneficial to induce a burst of nucleation and achieve complete conversion of zeolites in a short time. Bein and co-workers adopted this SAC method to synthesize the hierarchical Beta with varied Si/Al ratios from 10 to 33 at nearly 100% yield.[12] Despite the above advantages, the preparation process of dry gel powder is complicated and still requires a lot of water. We propose that combining steam-assisted crystallization with a solvent-free route would be a promising synthesis strategy for preparing highly dispersed nanosized hierarchical zeolites without forming bulky aggregates and producing wastewater.

In this work, we develop a steam-assisted crystallization procedure based on ball-milled solid raw materials for preparing highly dispersed nanosized hierarchical Beta zeolite. Different from the previous SAC method and solvent-free route, in this procedure, solid raw materials including Beta seed were mixed by mechanical ball-milling and then underwent the SAC process. The final nanosized product presents mulberry-like zeolite aggregates in size of *ca.* 200 nm that are assembled from uniform 15 nm crystallites, giving rise to abundant intraparticle interconnected mesopores. By this strategy, Beta zeolites with Si/Al ratios between 10 and 40 are synthesized by regulating the crystallization conditions. The crystallization process study reveals that the sufficient mixing of solid raw materials under ball-milling and favorable migration of solid mixture under steam conditions account for the construction of nanoparticles and intraparticle mesopores. Such a strategy can also be extended to the synthesis of nanosized hierarchical ZSM-5 zeolites. The present work provides a general strategy for the simple and cost-efficient synthesis of highly dispersed nanosized hierarchical zeolites, which will promise them superior catalytic properties.

Results and discussion

The synthesis procedure of nanosized hierarchical Beta zeolites *via* steam-assisted crystallization procedure based on ball-milled solid raw materials is illustrated in Scheme 1. Typically, a mixture of tetraethyl ammonium bromide (TEABr), solid silica gel, sodium aluminate, sodium hydroxide, and distilled water with a molar composition of $1.0SiO_2 : (0.0125–0.05)Al_2O_3 : (0.117–0.167)Na_2O : 0.28TEABr : 3.0H_2O$ was mixed with 10 wt% seed (relative to silica source) by ball-milling followed by steam-assisted crystallization. The products are denoted as Beta-*x*-BM-SAC, in which *x* indicates the initial Si/Al ratio in the mixture ($x = 10$, 20, and 40). The detailed synthetic conditions are listed in Table S1.† Furthermore, Beta-20-BM-HT, Beta-20 MG-SAC, and Beta-20 MG-HT zeolites prepared by different mixing methods including ball-milling (BM) and manual grinding (MG) and crystallization approaches including steam-assisted crystallization (SAC) and heating treatment (HT) were also compared to investigate the effect of mixing methods and crystallization approaches on the properties of Beta zeolites.

Scheme 1 The synthesis procedure of nanosized hierarchical Beta zeolite. Firstly, solid raw materials including solid silica gel, TEABr, sodium aluminate, sodium hydroxide, Beta seed, and distilled water were mixed into a ball-milling jar. After mechanical mixing for 5 h, the powder mixture was transferred into a Teflon cup for crystallization at 140 °C for 3 days, during which the water necessary for crystallization was kept separate from the solid mixtures. Upon centrifugation, drying, and calcination, nanosized hierarchical zeolite Beta can be finally obtained.

As shown in the powder X-ray (PXRD) diffraction (Fig. 1 and S1†), all samples show the characteristic peaks corresponding to Beta zeolite and no other diffraction peaks are observed. Beta-20-BM-SAC prepared *via* steam-assisted crystallization from ball-milled solid mixtures exhibits a relatively high crystallinity of 94% among all the samples. Whereas the relative crystallinities of Beta-20-BM-HT, Beta-20-MG-SAC, and Beta-20-MG-HT zeolites are 100%, 82%, and 77%, respectively. It can be seen from the scanning electron microscopy (SEM) images that these four samples exhibit completely different crystal morphologies (Fig. 1a–h). Notably, Beta-20-BM-SAC are uniformly dispersed nanosized crystals with a particle size of *ca.* 200 nm (Fig. 1a and b). Beta-20-BM-HT are aggregates (~1 μm) assembled from dipyramids with a particle size of *ca.* 250 nm (Fig. 1c and d), which is due to the low migration rate of solid mixture precursors under heating treatment. In comparison, although the enhanced migration rate with the assistance of steam is conducive to producing small-sized particles, Beta-20-MG-SAC presents serious agglomeration formed by the packing of nanoparticles (~30 nm) (Fig. 1e and f). Furthermore, Beta-20-MG-HT appears more serious bulky agglomeration consisting of particles with size of *ca.* 300 nm (Fig. 1g and h). By comparing the four Beta zeolites prepared through different mixing methods and crystallization approaches, it is found that ball-milling can facilitates more sufficient and uniform mixing of solid raw materials than manual grinding while steam-assisted crystallization could enhance the migration rate of solid mixture compared to heating treatment under solvent-free conditions. Therefore, it could be concluded that the construction of homogeneous nanosized Beta zeolite samples with high crystallinity and good dispersion can only be achieved by simultaneously combining the ball-milling and steam-assisted crystallization.

The morphologies and structures of Beta-*x*-BM-SAC zeolites prepared by steam-assisted crystallization from ball-milled solid mixtures were further characterized by various electron microscopy techniques. Low-voltage high-resolution scanning electron microscopy (LV-HR-SEM) images of Beta-20-BM-SAC (Fig. 2a and b) and scanning transmission electron microscopy-secondary electron imaging (STEM-SEI) images of Beta-10-BM-SAC and Beta-40-BM-SAC (Fig. S2a and b†) show

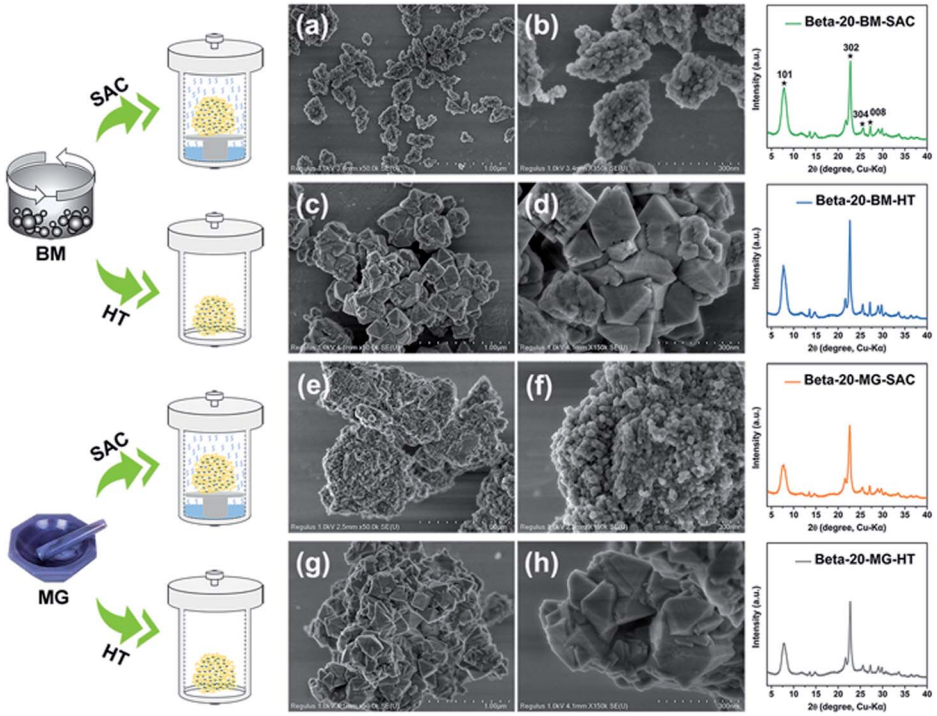

Fig. 1 SEM images and PXRD patterns of Beta zeolites synthesized by different synthesis methods: (a and b) Beta-20-BM-SAC, (c and d) Beta-20-BM-HT, (e and f) Beta-20-MG-SAC, and (g and h) Beta-20-MG-HT.

that these Beta zeolites present mulberry-like morphologies, and each mulberry-like crystal is assembled from nanoparticles in a size of *ca.* 15 nm. Fig. S3† exhibits the transmission electron microscopy (TEM) images of these Beta zeolites, in which abundant intraparticle mesopores are observed. These intraparticle mesopores are further proved to be interconnected by scanning transmission electron microscopy-high angle annular dark field (STEM-HAADF) images (Fig. 2c, S2c and d†). Different from the sample prepared by traditional steam-assisted conversion which contains interparticle mesopores,[12] the mesopores formed here are intraparticle interconnected mesopores. Movies corresponding to electron tomography reconstruction are provided as additional evidence of interconnected mesoporous structure in the ESI (Videos S1 and S2†).

Furthermore, the hysteresis loops at P/P_0 between 0.6 and 1.0 in the N_2 adsorption/desorption isotherms confirm the existence of abundant mesopores in Beta-*x*-BM-SAC samples (Fig. 2d and S4a†). The pore size distributions indicate their hierarchical porosities feature with a gradient from 6 nm to 15 nm (Fig. 2d and S4b†). Notably, these nanosized hierarchical Beta zeolites possess large surface areas (569–610 $m^2\ g^{-1}$) and large mesopore volumes (0.55–0.67 $cm^3\ g^{-1}$), which are comparable to those of mesoporous Beta zeolites obtained by conventional hydrothermal synthesis strategies.[13] By contrast, Beta-20-BM-HT, Beta-20-MG-SAC, and Beta-20-MG-HT possess lower surface areas (447–500 $m^2\ g^{-1}$) and mesopore volumes (0.07–0.25 $cm^3\ g^{-1}$) than Beta-20-BM-SAC (Table 1), which is consistent with the weak hysteresis loops observed in Fig. S5.† The temperature-programmed desorption of ammonia (NH_3-TPD) analysis results show that the total acidities of three nanosized hierarchical Beta samples decrease with the increase of Si/Al ratios (Fig. S6†). ^{29}Si MAS NMR results demonstrate that these samples contain a small amount of Q^3 corresponds to SiOH sites while most of the Si species belong to Q^4 (4Si, 0Al) (Fig. 1e and S7†). ^{27}Al MAS NMR spectra show more than 80% aluminum exist in the form of tetrahedral coordination (Fig. 1f and S7†).

To assess the hydrothermal stability of Beta-20-BM-SAC, the sample was exposed to 10% water steaming at 750 °C for 3 h. After hydrothermal treatment, Beta-20-BM-SAC shows a nearly unchanged PXRD pattern, N_2 adsorption/desorption isotherm, ^{27}Al MAS NMR spectrum, NH_3-TPD profile, and TEM image (Fig. S8–S12†), indicating its superior hydrothermal stability. Above results clearly indicate that the steam-assisted crystallization from ball-milled solid mixtures is an effective approach for the synthesis of highly dispersed nanosized hierarchical Beta zeolites with large mesopore volume and good hydrothermal stability.

To investigate the effects of synthetic parameters on the formation of nanosized hierarchical zeolites under such steam-assisted crystallization conditions, the H_2O/SiO_2 ratio, seed addition, and ball-milling time were adjusted to prepare a series of Beta-20-BM-SAC samples. The detailed characterizations are shown in ESI (Fig. S13–S20†).

Impact of the H_2O/SiO_2 ratio on morphology and structure

Beta-20-BM-SAC-*y* samples (*y* indicates the H_2O/SiO_2 ratio, y = 0, 1.5, 6) were synthesized to investigate the effect of H_2O/SiO_2 ratio on the crystallization process. It can be seen from the

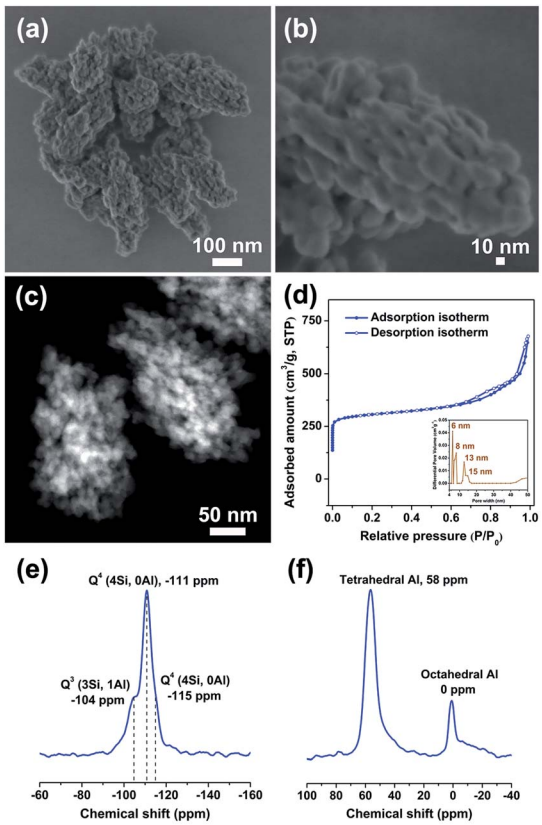

Fig. 2 Morphology and structure characterizations of Beta-20-BM-SAC zeolite. (a) Low-magnification LV-HR-SEM image, (b) high-magnification LV-HR-SEM image, (c) high-magnification STEM-HAADF image, (d) N_2 adsorption/desorption isotherm and pore size distribution (inset), (e) ^{29}Si solid-state MAS NMR spectrum, and (f) ^{27}Al solid-state MAS NMR spectrum.

PXRD patterns that all the samples are ***BEA**-type zeolite regardless of the amount of water added to the solid mixture (Fig. S13†). When decreasing the H_2O/SiO_2 ratio to 0, as-prepared Beta-20-BM-SAC-0 shows a blocky aggregation state (Fig. S14a and d†). In contrast, Beta-20-BM-SAC-1.5 zeolite presents mulberry-like aggregates assembled from nanoparticles (~15 nm) in a compact packing manner (Fig. S14b and e†). While for Beta-20-BM-SAC-6, similar aggregates like Beta-20-BM-SAC-0.5 are assembled in a non-compact manner, resulting in the construction of intraparticle mesopores (Fig. S14c and f†).

Impact of the seed addition on morphology and structure

The H-Beta seed used in this work was commercial Beta zeolite with a Si/Al ratio of 12.5 (denoted as Beta-Com), which possesses a relative low crystallinity (Fig. S15a†) and presents an aggregated state assembled from 20 nm nanosized crystallites (Fig. S16a†). After the ball-milling for 5 h, the Beta-Com presents an XRD amorphous phase (Fig. S15b†) and irregular morphology (Fig. S16b†), indicating that its crystal structure has been destroyed during the mechanical ball-milling process. To investigate the effect of seed addition on the crystallization process, Beta-20-BM-SAC-*z* samples were prepared where *z* represents the seed addition (z = 0 wt%, 5 wt%, and 20 wt%, which are relative to silica source). All the samples are ***BEA**-type zeolite as confirmed by PXRD analysis (Fig. S17†). When no Beta seed is added to the solid raw materials, Beta-20-BM-SAC-0 wt% presents blocky aggregates with a micron crystal size of 1 μm and possesses a pure microporous structure (Fig. S18a and d†). Increasing the seed addition to 5 wt%, Beta-20-BM-SAC-5 wt% shows well-dispersed aggregates with a smaller crystal size of 200 nm (Fig. S18b and e†). When the seed addition is large enough to be 20 wt%, Beta-20-BM-SAC-20 wt% are nanocrystals with a size of 15 nm (Fig. S18c and f†).

Impact of the ball-milling time on morphology and structure

Beta-20-BM-SAC-*m* samples (*m* indicates the ball-milling time (h), m = 1/3, 1, 8) were synthesized to investigate the effect of ball-milling time on the crystallization process. Beta-20-BM-SAC-1/3, Beta-20-BM-SAC-1, and Beta-20-BM-SAC-8 are all ***BEA**-type zeolites as confirmed by PXRD analysis (Fig. S19†). In a short ball-milling time of 1/3 h, the uneven mixing of solid raw materials leads to the serious aggregation of mixtures, resulting in a blocky morphology for Beta-20-BM-SAC-1/3 (Fig. S20a and d†). Increasing the ball-milling time to 1 h, the crystal size of Beta-20-BM-SAC-1 is greatly reduced but remains uneven (Fig. S20b and e†). Unlike the well-dispersed nanosized

Table 1 Textural properties of as-prepared Beta zeolites and ZSM-5 zeolites

Sample	R^a	$S_{BET}{}^b$ ($m^2\ g^{-1}$)	$S_{ext}{}^c$ ($m^2\ g^{-1}$)	$V_{micro}{}^c$ ($cm^3\ g^{-1}$)	$V_{meso}{}^d$ ($cm^3\ g^{-1}$)
Beta-10-BM-SAC	—	586	248	0.19	0.55
Beta-40-BM-SAC	—	569	233	0.19	0.61
Beta-20-BM-SAC	94	610	235	0.18	0.67
Beta-20-BM-SAC-HT[e]	91	567	222	0.17	0.53
Beta-20-BM-HT	100	500	126	0.20	0.25
Beta-20-MG-SAC	82	485	115	0.16	0.10
Beta-20-MG-HT	77	447	84	0.15	0.07
ZSM-5-20-BM-SAC	—	420	111	0.12	0.18
ZSM-5-20-Con	—	354	70	0.11	0.16

[a] Relative crystallinity calculated based on the intensity of the peaks at 2θ of 7.6° and 22.6°. The Beta-20-BM-HT is considered as a reference. [b] S_{BET}: total surface area, calculated by the BET method. [c] S_{ext}: external surface area, and V_{micro}: micropore volume, calculated by the *t*-plot method. [d] V_{meso}: mesopore volume, $V_{meso} = V_{total} - V_{micro}$. [e] Beta-20-BM-SAC sample after hydrothermal treatment.

hierarchical structure of Beta-20-BM-SAC synthesized with ball-milling time of 5 h, Beta-20-BM-SAC-8 presents aggregates assembled from nanocrystals (Fig. S20c and f†), which is due to the secondary aggregation of solid mixture caused by excessive mechanical mixing under 8 h ball-milling. Based on these results, it can be concluded that the H_2O/SiO_2 ratios of 3, seed addition of 10 wt%, and a ball-milling time of 5 h are conducive to the construction of a highly dispersed nanosized hierarchical structure of Beta zeolites.

To investigate the evolution process of Beta-20-BM-SAC, Beta-20-BM-SAC-*n* intermediates were synthesized at different crystallization periods from 0 h to 72 h, where *n* represents the crystallization time. Beta-20-BM-SAC-0h, the initial mixture of solid raw materials, shows an XRD amorphous phase (Fig. S21†) and spherical morphology with a particle size of *ca.* 20 nm (Fig. 3a and S22a†). After 12 h of crystallization, Beta-20-BM-SAC-12h still appears XRD amorphous phase (Fig. S21†). It was worth noting that Beta-20-BM-SAC-0h aggregated in a non-compact manner to form Beta-20-BM-SAC-12h aggregates that maintain a certain particle size of *ca.* 200 nm, which was limited by the hydrated layer surrounding the solid mixture (Fig. 3b and S22c†). Meanwhile, the concentration fluctuation combined with the assistance of seed induced the formation of numerous nucleation centers. At this stage, stacking voids were produced in Beta-20-BM-SAC-12h because of the non-compact accumulation, affording a mesopore volume of 0.27 $cm^3\ g^{-1}$ (Fig. S23 and Table S2†). With prolonging the crystallization time to 15 h, the crystalline ***BEA** feature is observed in Beta-20-BM-SAC-15h (Fig. S21†), indicating the onset of crystallization. As shown in Fig. 3c and S22d,† Beta-20-BM-SAC-12h aggregates were transformed into integrated Beta-20-BM-SAC-15h dense intermediates through contraction and densification, during which parts of the solid precursor are converted into nanocrystals in a short SAC treatment, generating abundant interstitial voids. Further increasing the crystallization time to 18 h, the crystallinity of the product increased greatly, indicating that residual nucleation sites were also gradually crystallized into nanocrystals with ***BEA** feature under continuous SAC reaction. The formed small-sized nanocrystals in Beta-20-BM-SAC-18h migrated and rearranged into an aggregated network with the assistance of a hydrated layer, resulting in the transformation of interstitial voids into isolated mesopores (Fig. 3d and S22e†) and the mesopore volume of Beta-20-BM-SAC-18h increased to 0.48 $cm^3\ g^{-1}$ (Fig. S23 and Table S2†). As the crystallization time further increasing to 72 h, the crystallization was completed and the crystallinity of Beta-20-BM-SAC-72h reached the highest (Fig. S21†). Under such steam-assisted conditions, the nanocrystals formed in the early stages coalesced into larger uniform nanoparticles through intraparticle ripening, avoiding the excessive growth induced by Ostwald ripening. The resulting Beta-20-BM-SAC-72h show mulberry-like morphologies and is assembled from uniform nanoparticles with a particle size of *ca.* 15 nm, simultaneously abundant intraparticle interconnected mesopores are constructed through the evolution of primarily isolated mesopores (Fig. 2d, 3e and S22f† and Table 1). According to the above results, the crystallization process of Beta-20-BM-SAC and interconnected intraparticle mesopore formation mechanism are proposed in Fig. 3f. At the initial stage of crystallization, the solid mixture aggregated in a non-compact manner and then contracted, affording abundant interstitial voids within integrated intermediates. Subsequently, the rearrangement of nanocrystals induced the formation of isolated mesopores, which further evolved into interconnected intraparticle mesopores through the sustaining coalescence of nanocrystals.

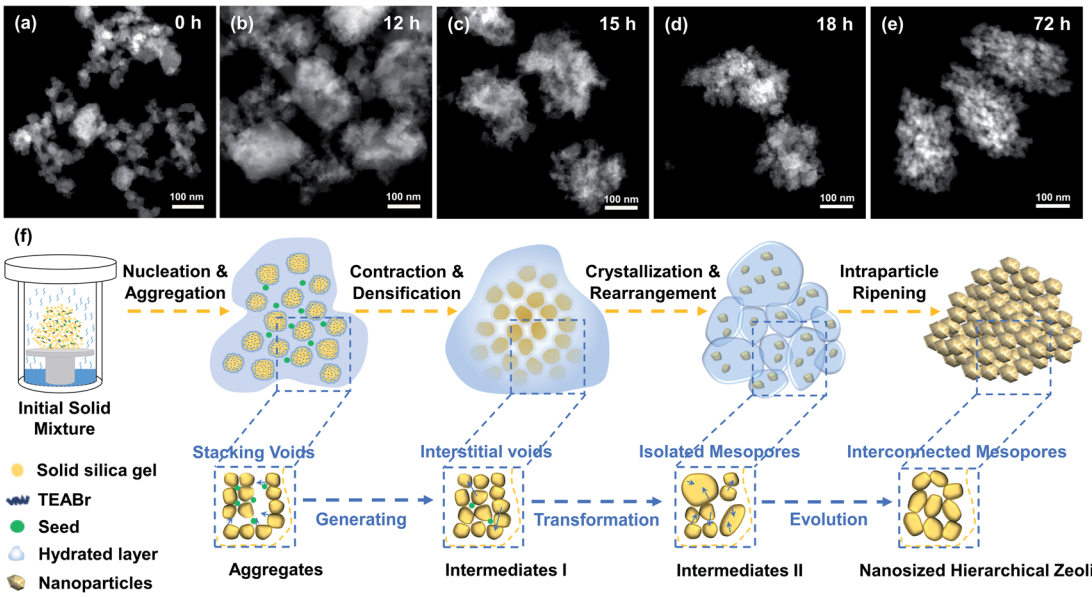

Fig. 3 The steam-assisted crystallization process of Beta-20-BM-SAC. (a–e) STEM-HAADF images of Beta-20-BM-SAC crystalline evolved under 140 °C at different periods (0–72 h). (f) Schematic illustration of steam-assisted crystallization process based on solid raw materials and the formation of intraparticle mesopores.

To demonstrate the generality of the steam-assisted crystallization strategy based on ball-milled solid raw materials, nanosized hierarchical ZSM-5 zeolite was also synthesized through this method. Typically, a mixture of tetrapropyl ammonium bromide (TPABr), solid silica gel, sodium aluminate, sodium hydroxide, and distilled water with a molar composition of $1.0SiO_2 : 0.025Al_2O_3 : 0.083Na_2O : 0.28TPABr : 3H_2O$ was firstly mixed with 10 wt% seed (relative to silica source) by ball-milling for 5 h, then crystallized at 160 °C for 72 h. The H-ZSM-5 seed was commercial ZSM-5 zeolite with a Si/Al ratio of 20. It possesses a good crystallinity (Fig. S24†) and displays micron-sized crystals (*ca.* 2 μm) with rough surface (Fig. S25†). As-prepared ZSM-5 zeolite is denoted as ZSM-5-20-BM-SAC. The detailed synthetic conditions are listed in Table S1.† As confirmed by PXRD analysis, the sample is **MFI**-type zeolite (Fig. 4g). As shown in Fig. 4a, ZSM-5-20-BM-SAC displays uniformly dispersed crystals in a particle size of *ca.* 700 nm. High-magnification LV-HR-SEM image of ZSM-5-20-BM-SAC further shows that the sample presents virus-like aggregates assembled from uniform nanoparticles (~30 nm) (Fig. 4d). As seen in the TEM images (Fig. 4b and e), ZSM-5-20-BM-SAC is rich in intraparticle mesopores, which are further confirmed to be interconnected mesopores by STEM-HAADF images (Fig. 4c and f). The ED pattern corresponding to the entire particle reveals the polycrystalline feature of ZSM-5-20-BM-SAC. For comparison, conventional ZSM-5 zeolite (ZSM-5-20-Con) was synthesized in a starting gel of tetrapropylammonium hydroxide, tetraethylorthosilicate, sodium aluminate, and sodium hydroxide with the molar composition of $1.0SiO_2 : 0.30TPAOH : 0.025Al_2O_3 : 0.015Na_2O : 50H_2O$ under hydrothermal conditions at 170 °C for 72 h. SEM images of ZSM-5-20-Con show that it presents spherical crystals that are formed by the compact accumulation of small particles (Fig. S26†). The N_2 adsorption/desorption isotherms (Fig. S27†) also confirm the formation of mesopores and the nanosized hierarchical ZSM-5-20-BM-SAC zeolite shows a larger external surface area of 111 $m^2 g^{-1}$ than that of ZSM-5-20-Con zeolite (70 $m^2 g^{-1}$) (Table 1). The ^{29}Si MAS NMR spectrum shows that ZSM-20-BM-SAC consists a small amount of a Q^3 (3Si, 1Al) and a majority of Q^4 (4Si, 0Al) (Fig. 4h). ^{27}Al MAS NMR spectrum shows that ZSM-20-BM-SAC only possesses tetrahedral framework Al species (Fig. 4i). This steam-assisted crystallization strategy based on ball-milled solid raw materials is universal to prepare nanosized hierarchical Beta and ZSM-5 zeolites and is expected to be expanded to other framework types of zeolites.

As-prepared nanosized hierarchical Beta zeolites were applied in the catalytic conversion of high-concentrated lactic acid (LA, 105 wt%) to lactide (LT) (Fig. 5a). Due to the good shape-selective property of Beta zeolite, the Beta zeolite-based catalytic route has been developed for the efficient production of lactide from lactic acid, which is highly desired for further production of biodegradable and renewable polylactic acid (PLA).[14] Nanosized hierarchical Beta-*x*-BM-SAC zeolites were compared with Beta-20-BM-HT, Beta-20-MG-SAC, Beta-20-MG-HT, and Beta-Com (Si/Al = 12.5, Alfa Aesar Company) zeolites in this biomass conversion reaction. Among the four Beta zeolites (Beta-20-BM-SAC, Beta-20-BM-HT, Beta-20-MG-SAC, and Beta-20-MG-HT) with a comparable Si/Al ratio of 17.3–18.1 (Table S1†), nanosized hierarchical Beta-20-BM-SAC gave the highest LT yield of 75.7% while the other three Beta zeolites

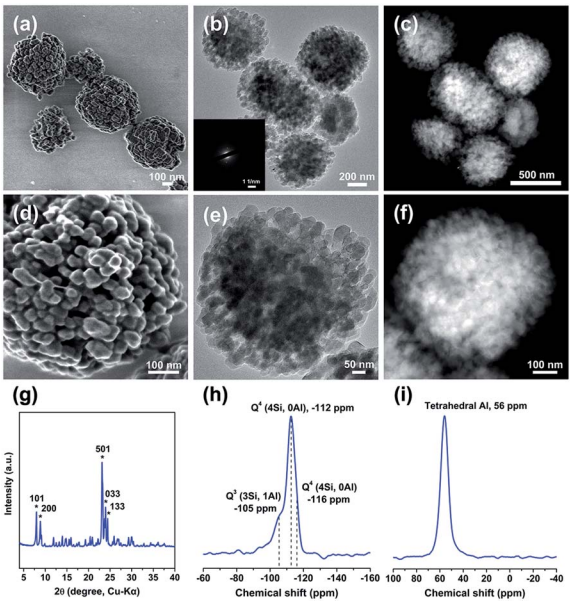

Fig. 4 Morphology and structure characterizations of ZSM-5-20-BM-SAC. (a) Low-magnification LV-HR-SEM image, (b) low-magnification TEM image, (c) low-magnification STEM-HAADF image, (d) high-magnification LV-HR-SEM image, (e) high-magnification TEM image, (f) high-magnification STEM-HAADF image, (g) PXRD pattern, (h) ^{29}Si solid-state MAS NMR spectrum, and (i) ^{27}Al solid-state MAS NMR spectrum. Inset: corresponding ED patterns obtained from the entire particles.

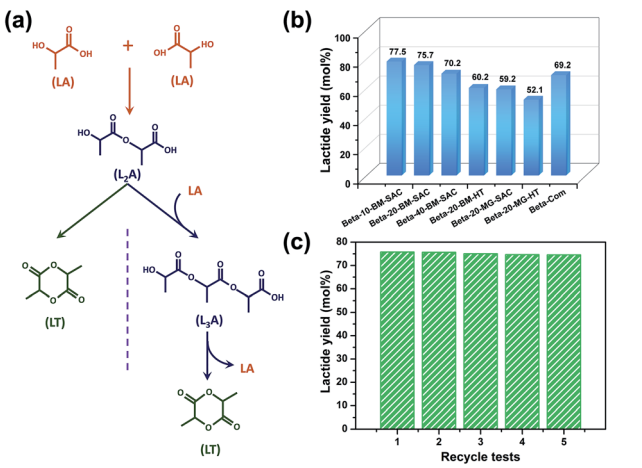

Fig. 5 Catalytic performance of various Beta zeolite catalysts in the catalytic conversion of lactic acid to lactide. (a) Scheme of reaction pathways of lactic acid to lactide, (b) lactide yield after reaction of 5 h based on ^1H-NMR analysis over different Beta zeolite catalysts, and (c) recycle tests for production of lactide over catalyst Beta-20-BM-SAC. Reaction conditions: 1.0 g catalyst, 1.0 g 105 wt% LA, 20 mL toluene, 140 °C, 5 h.

showed a low LT yield of 52.1–60.2% (Fig. 5b and S28†). For three nanosized hierarchical Beta zeolites prepared by steam-assisted crystallization from ball-milled solid mixture, Beta-10-BM-SAC with the maximum acidities gave the highest LT yield of 77.5%, which was also superior to that of Beta-Com (69.2%) with a similar Si/Al ratio and crystal size. Above results evidently reveal the advantages of intraparticle interconnected mesopores for Beta-*x*-BM-SAC zeolites in the catalytic conversion of lactic acid to lactide, which enhances the diffusion properties of macromolecular products. Besides, the ^{1}H-NMR time profiles of LA conversion over Beta-20-BM-SAC zeolite confirmed that both L_2A and L_3A acted as reaction intermediates (Fig. S29†), which is in line with our previous work.[15] Notably, after five recycles of conversion of lactic acid, nanosized hierarchical Beta-20-BM-SAC zeolite still maintained a high LT yield without an obvious loss in the activity (Fig. 5c), revealing the excellent cyclic stability of nanosized hierarchical Beta zeolites. It is worth noting that the catalyst remains a good crystallinity (Fig. S30†) and presents the same aggregated morphology as the pristine catalyst (Fig. S31†), indicating its outstanding mechanical stability under the reaction conditions.

Conclusions

In summary, we have developed a facile steam-assisted crystallization strategy based on ball-milled solid raw materials for synthesizing highly dispersed nanosized hierarchical Beta zeolites. Such an approach exhibits significant advantages: (1) lower synthesis cost than hydrothermal synthesis, due to using TEABr and TPABr as templates and using solid silica gel as silica source. (2) Simpler synthesis procedure than traditional SAC method, by directly using mechanical mixing solid raw materials instead of preparing drying gel precursor. (3) Higher dispersion and uniformity of crystals than those obtained in the solvent-free route, due to the sufficient and even mixing under ball-milling rather than manual grinding. (4) Generation of nanoparticles in a size of *ca.* 15 nm, due to the steam-saturated condition. (5) Formation of interconnected intraparticle mesopores, achieved by the initial aggregation of solid mixture in a non-compact manner and subsequently intraparticle ripening of nanocrystals. Very importantly, the as-prepared Beta zeolites show excellent catalytic activity and stability in the conversion of LA to LT reaction. This strategy opens up a new avenue for the cost-effective synthesis of highly dispersed nanosized hierarchical zeolites with large mesopore volume and good hydrothermal stability that can be used in various important catalytic reactions. Such a synthetic strategy can be also extended to the synthesis of nanosized hierarchical zeolites with other structure types (*e.g.*, **MFI**-type) and with metal active sites (*e.g.*, Ti, Fe).

Author contributions

Prof. J. H. Y. conceived the project. Z. M. designed and performed experiments, characterized samples, performed the catalysis reactions, analyzed data and wrote the manuscript. L. L. performed TEM and STEM-HAADF images analysis. M. Y. C. performed SEM images analysis. J. Y. L. performed STEM-SEI images analysis and electron tomography reconstruction. Q. Z. provided some suggestions to improve the work. All authors discussed the results and commented on the manuscript. Prof. J. H. Y. revised the manuscript and finalized the manuscript.

Conflicts of interest

There are no conflicts to declare.

Acknowledgements

We thank the National Key Research and Development Program of China (Grant 2021YFA1501202), the National Natural Science Foundation of China (Grant 21920102005, 21835002 and 21621001), and the 111 Project (B17020) for supporting this work. The Centre for High-resolution Electron Microscopy (C*ħ*EM), supported by SPST of ShanghaiTech University under Contract EM02161943 is acknowledged for their help on electron microscopy.

Notes and references

1 (*a*) G. Feng, P. Cheng, W. Yan, M. Boronat, X. Li, J.-H. Su, J. Wang, Y. Li, A. Corma and R. Xu, *Science*, 2016, **351**, 1188–1191; (*b*) Q. Zhang, A. Mayoral, O. Terasaki, Q. Zhang, B. Ma, C. Zhao, G. Yang and J. Yu, *J. Am. Chem. Soc.*, 2019, **141**, 3772–3776; (*c*) S. Shevlin, *Nat. Mater.*, 2020, **19**, 1038–1039; (*d*) M. Van den Bergh, A. Krajnc, S. Voorspoels, S. R. Tavares, S. Mullens, I. Beurroies, G. Maurin, G. Mali and D. E. De Vos, *Angew. Chem., Int. Ed.*, 2020, **132**, 14190–14194.

2 (*a*) E. T. Vogt and B. M. Weckhuysen, *Chem. Soc. Rev.*, 2015, **44**, 7342–7370; (*b*) D. Fu, A. Lucini Paioni, C. Lian, O. van der Heijden, M. Baldus and B. M. Weckhuysen, *Angew. Chem., Int. Ed.*, 2020, **59**, 20024–20030; (*c*) W. Dai, C. Kouvatas, W. Tai, G. Wu, N. Guan, L. Li and V. Valtchev, *J. Am. Chem. Soc.*, 2021, **143**, 1993–2004; (*d*) M. H. Sun, L. H. Chen, S. Yu, Y. Li, X. G. Zhou, Z. Y. Hu, Y. H. Sun, Y. Xu and B. L. Su, *Angew. Chem., Int. Ed.*, 2020, **132**, 19750–19759; (*e*) Z. Guo, X. Li, S. Hu, G. Ye, X. Zhou and M. O. Coppens, *Angew. Chem., Int. Ed.*, 2020, **132**, 1564–1567; (*f*) Y. Chen, K. Gong, F. Jiao, X. Pan, G. Hou, R. Si and X. Bao, *Angew. Chem., Int. Ed.*, 2020, **132**, 6591–6596; (*g*) E. M. Gallego, C. Paris, M. R. Díaz-Rey, M. E. Martínez-Armero, J. Martínez-Triguero, C. Martínez, M. Moliner and A. Corma, *Chem. Sci.*, 2017, **8**, 8138–8149; (*h*) R. Martínez-Franco, C. Paris, M. E. Martínez-Armero, C. Martínez, M. Moliner and A. Corma, *Chem. Sci.*, 2016, **7**, 102–108.

3 (*a*) E. R. Cooper, C. D. Andrews, P. S. Wheatley, P. B. Webb, P. Wormald and R. E. Morris, *Nature*, 2004, **430**, 1012–1016; (*b*) M. Choi, K. Na, J. Kim, Y. Sakamoto, O. Terasaki and R. Ryoo, *Nature*, 2009, **461**, 246–249; (*c*) K. Na, C. Jo, J. Kim, K. Cho, J. Jung, Y. Seo, R. J. Messinger, B. F. Chmelka and R. Ryoo, *Science*, 2011, **333**, 328–332; (*d*) J. Sun, C. Bonneau, Á. Cantín, A. Corma, M. J. Díaz-Cabañas, M. Moliner, D. Zhang, M. Li and X. Zou, *Nature*, 2009, **458**, 1154–1157; (*e*) R. Cai, M. Sun, Z. Chen,

R. Munoz, C. O'Neill, D. E. Beving and Y. Yan, *Angew. Chem., Int. Ed.*, 2008, **47**, 525–528; (*f*) E. R. Parnham and R. E. Morris, *J. Am. Chem. Soc.*, 2006, **128**, 2204–2205; (*g*) T.-H. Bae, J. Liu, J. S. Lee, W. J. Koros, C. W. Jones and S. Nair, *J. Am. Chem. Soc.*, 2009, **131**, 14662–14663; (*h*) R. I. Walton, *Chem. Soc. Rev.*, 2002, **31**, 230–238; (*i*) I. Julian, M. B. Roedern, J. L. Hueso, S. Irusta, A. K. Baden, R. Mallada, Z. Davis and J. Santamaria, *Appl. Catal., B*, 2020, **263**, 118360.

4 (*a*) Q. Wu, X. Meng, X. Gao and F.-S. Xiao, *Acc. Chem. Res.*, 2018, **51**, 1396–1403; (*b*) R. E. Morris and S. L. James, *Angew. Chem., Int. Ed.*, 2013, **52**, 2163–2165; (*c*) X. Meng and F.-S. Xiao, *Chem. Rev.*, 2014, **114**, 1521–1543; (*d*) X. Meng, Q. Wu, F. Chen and F.-S. Xiao, *Sci. China: Chem.*, 2015, **58**, 6–13; (*e*) L. Zhu, J. Zhang, L. Wang, Q. Wu, C. Bian, S. Pan, X. Meng and F.-S. Xiao, *J. Mater. Chem. A*, 2015, **3**, 14093–14095.

5 Y. Jin, Q. Sun, G. Qi, C. Yang, J. Xu, F. Chen, X. Meng, F. Deng and F. S. Xiao, *Angew. Chem., Int. Ed.*, 2013, **52**, 9172–9175.

6 (*a*) Y. Jin, X. Chen, Q. Sun, N. Sheng, Y. Liu, C. Bian, F. Chen, X. Meng and F. S. Xiao, *Chem.–Eur. J.*, 2014, **20**, 17616–17623; (*b*) X. Chen, X. Meng and F.-s. Xiao, *Chin. J. Catal.*, 2015, **36**, 797–800; (*c*) N. Sheng, Y. Chu, S. Xin, Q. Wang, X. Yi, Z. Feng, X. Meng, X. Liu, F. Deng and F.-S. Xiao, *J. Am. Chem. Soc.*, 2016, **138**, 6171–6176.

7 (*a*) L. Ren, Q. Wu, C. Yang, L. Zhu, C. Li, P. Zhang, H. Zhang, X. Meng and F.-S. Xiao, *J. Am. Chem. Soc.*, 2012, **134**, 15173–15176; (*b*) X. Wang, Q. Wu, C. Chen, S. Pan, W. Zhang, X. Meng, S. Maurer, M. Feyen, U. Müller and F.-S. Xiao, *Chem. Commun.*, 2015, **51**, 16920–16923; (*c*) Q. Wu, X. Liu, L. Zhu, L. Ding, P. Gao, X. Wang, S. Pan, C. Bian, X. Meng and J. Xu, *J. Am. Chem. Soc.*, 2015, **137**, 1052–1055.

8 Q. Wu, X. Wang, G. Qi, Q. Guo, S. Pan, X. Meng, J. Xu, F. Deng, F. Fan and Z. Feng, *J. Am. Chem. Soc.*, 2014, **136**, 4019–4025.

9 H. Li, X. Liu, S. Qi, L. Xu, G. Shi, Y. Ding, X. Yan, Y. Huang and J. Geng, *Angew. Chem., Int. Ed.*, 2017, **129**, 14278–14283.

10 (*a*) P. H. PrasadáRao, *Chem. Commun.*, 1996, 1441–1442; (*b*) B. Chen and Y. Huang, *J. Am. Chem. Soc.*, 2006, **128**, 6437–6446; (*c*) X. Cheng, J. Mao, X. Lv, T. Hua, X. Cheng, Y. Long and Y. Tang, *J. Mater. Chem. A*, 2014, **2**, 1247–1251; (*d*) C.-C. Chang, H. J. Cho, Z. Wang, X. Wang and W. Fan, *Green Chem.*, 2015, **17**, 2943–2951; (*e*) X. He, T. Ge, Z. Hua, J. Zhou, J. Lv, J. Zhou, Z. Liu and J. Shi, *ACS Appl. Mater. Interfaces*, 2016, **8**, 7118–7124; (*f*) V. Vattipalli, A. M. Paracha, W. Hu, H. Chen and W. Fan, *Angew. Chem., Int. Ed.*, 2018, **57**, 3607–3611; (*g*) Y. Luo, Y. Zhu, J. Pan and X. Chen, *Green Chem.*, 2020, **22**, 1681–1697.

11 J. Zhang, P. Cao, H. Yan, Z. Wu and T. Dou, *Chem. Eng. J.*, 2016, **291**, 82–93.

12 K. Möller, B. Yilmaz, R. M. Jacubinas, U. Müller and T. Bein, *J. Am. Chem. Soc.*, 2011, **133**, 5284–5295.

13 (*a*) J. Zhu, Y. Zhu, L. Zhu, M. Rigutto, A. van der Made, C. Yang, S. Pan, L. Wang, L. Zhu and Y. Jin, *J. Am. Chem. Soc.*, 2014, **136**, 2503–2510; (*b*) M. H. Sun, L. H. Chen, S. Yu, Y. Li, X. G. Zhou, Z. Y. Hu, Y. H. Sun, Y. Xu and B. L. Su, *Angew. Chem., Int. Ed.*, 2020, **132**, 19750–19759.

14 M. Dusselier, P. Van Wouwe, A. Dewaele, P. A. Jacobs and B. F. Sels, *Science*, 2015, **349**, 78–80.

15 Q. Zhang, S. Xiang, Q. Zhang, B. Wang, A. Mayoral, W. Liu, Y. Wang, Y. Liu, J. Shi and G. Yang, *Chem. Mater.*, 2019, **32**, 751–758.